Applied Catalysis B: Environmental 306 (2022) 121127

Contents lists available at ScienceDirect

Applied Catalysis B: Environmental

journal homepage: www.elsevier.com/locate/apcatb

Crystalline-amorphous interface of mesoporous Ni_2P @ $FePO_xH_y$ for oxygen evolution at high current density in alkaline-anion-exchange-membrane water-electrolyzer

Abhishek Meena [a,b,*], Pandiarajan Thangavel [a,**], Da Sol Jeong [a], Aditya Narayan Singh [a,c], Atanu Jana [a,b], Hyunsik Im [b], Duc Anh Nguyen [b], Kwang S. Kim [a,**]

[a] Center for Superfunctional Materials, Department of Chemistry, Ulsan National Institute of Science and Technology (UNIST), 50 UNIST-gil, Ulsan 44919, Republic of Korea

[b] Division of Physics and Semiconductor Science, Dongguk University, Seoul 04620, Republic of Korea

[c] Department of Energy and Materials Engineering, Dongguk University-Seoul, Seoul 04620, Republic of Korea

ARTICLE INFO

Keywords:
Energy conversion
Oxygen evolution reaction
Water-electrolyzer
High current density
Electrocatalysts

ABSTRACT

For industrial high-purity hydrogen production, it is essential to develop low-cost, earth-abundant, highly-efficient, and stable electrocatalysts which deliver high current density (j) at low overpotential (η) for oxygen evolution reaction (OER). Herein, we report an active mesoporous Ni_2P @ $FePO_xH_y$ pre-electrocatalyst, which delivers high j = 1 A cm^{-2} at η = 360 mV in 1 M KOH with long-term durability (12 days), fulfilling all the desirable commercial criteria for OER. The electrocatalyst shows abundant interfaces between crystalline metal phosphide and amorphous phosphorus-doped metal-oxide, improving charge transfer capability and providing access to rich electroactive sites. Combined with an excellent non-noble metal-based HER catalyst, we achieve commercially required j = 500/1000 mA cm^{-2} at 1.65/1.715 V for full water-splitting with excellent stability in highly corrosive alkaline environment (30% KOH). The alkaline-anion-exchange-membrane water-electrolyzer (AAEMWE) fabricated for commercial viability exhibits high j of 1 A cm^{-2} at 1.84 V with long-term durability as an economical hydrogen production method, outperforming the state-of-the-art Pt/C–IrO_2 catalyst.

1. Introduction

The rapid decline of fossil fuels raises an urgent call for finding an alternative means of clean, green, and renewable energy resources [1,2]. Among several alternative renewable energy technologies, splitting water to generate hydrogen for fuel is by far the most decent and viable technology that have gathered enormous interest in the recent few decades [1]. Industrial water-electrolyzers are a vital apparatus to produce pure hydrogen from water splitting. Alkaline anion and proton exchange membrane water-electrolyzers (AAEMWE and PEMWE) are primarily known as low-temperature water-electrolyzer technologies. Among the two electrolyzers, the AAEMWE electrolyzer in alkaline is much more demanded than the PEMWE electrolyzer in acid. This is mainly because the PEMWE electrolyzer mostly requires expensive noble metal iridium or platinum (Pt) based catalysts [3,4]. In contrast, the AAEMWE electrolyzer can be used for large-scale hydrogen production because the low-cost metals can be used as catalysts [5]. Researchers have recently developed a highly efficient AAEMWE electrolyzer using NiFe OER catalyst and an electrode binder with the highest ionic concentration to improve electrolyzer performance [3,4,6]. However, it shows poor stability, which limits its application in large-scale hydrogen production. As yet, water electrolysis contributes only less than 5% to global hydrogen production due to practical and economic issues with the electrolyzer fabrication technologies [3]. Therefore, the critical challenge is to develop highly efficient non-noble metal catalysts for large-scale water splitting with low cell voltages towards commercialization.

The OER is the essential counter half-cell reaction involved in overall water splitting. However, OER suffers from slow kinetics and high energy barrier (hence large η) of 4-electron oxidative half-cell reaction. Highly efficient OER catalysts are required to boost the overall water splitting [7,8]. The state-of-the-art RuO_2 and IrO_2 benchmark OER

* Corresponding author at: Division of Physics and Semiconductor Science, Dongguk University, Seoul 04620, Republic of Korea.
** Corresponding authors.
E-mail addresses: pakar.abhishek@gmail.com (A. Meena), pandiarajan@unist.ac.kr (P. Thangavel), kimks@unist.ac.kr (K.S. Kim).

https://doi.org/10.1016/j.apcatb.2022.121127
Received 26 June 2021; Received in revised form 16 January 2022; Accepted 19 January 2022
Available online 21 January 2022
0926-3373/© 2022 Elsevier B.V. All rights reserved.

catalysts have displayed their excellent performances [9]. However, their rocketing price nullifies its commercial viability. In the past few decades, significant efforts have been put to overcome the bottleneck OER in water splitting with reduced η by utilizing the transition metals (TMs) phosphides, sulfides, nitrides, chalcogenides, and thiophosphate materials [7,10]. In this regard, TMs phosphides (TMPs) have enormous potential as OER electrocatalysts due to their excellent electronic conductivity embedded in their intrinsic structures with an added advantage of their reduced prices [7,11–13].

Furthermore, bimetallic TMs bring exotic chemistry in OER. For instance, inclusions of Fe in Ni-based electrocatalysts dramatically modified the OER performances and brought about a 30-fold increment in film conductivity [14]. TMPs aggravate metal oxidation at high η, leading to the formation of unique core-shell structures of TM-P/TM-O_x, which assist in OER [15,16]. The TMP provides an obvious path to promote electronic conductivity, whereas TM-O_x serves as an OER active site [17]. Contrary to the monometallic TMPs, bimetallic TMPs significantly alter the electronic structures and improve the catalyst's OER performances [18]. Despite several benefits in bimetallic TMPs, their limited active sites restrict the utilization of their full potentials in water splitting reactions.

Additionally, bimetallic TMPs with porous nanostructure such as mesopores provide high surface area, indicating that a large number of active sites are exposed to the electrolyte. The high electrochemical surface area facilitates the adsorption/desorption process, resulting in improved catalytic activity [19]. Besides, the crystalline and amorphous phases in a single structure offer more catalytic active sites, accelerating the charge transfer and mass diffusion ability for highly efficient OER activity [20,21]. Most importantly, for large-scale industrial applications, OER catalysts need to deliver high $j \geq 500$ mA cm^{-2} at low $\eta \leq 300$ mV [4,22]. Only a few catalysts meet the above mentioned strict commercial criteria for OER, but they do not show the long-term durability for high j operation. Thus, it is imperative to rationally design bimetallic TMPs with numerous active sites to further enhance their electrochemical activities and durability.

Herein, we report the design and synthesis of novel cost-effective Ni_2P @ $FePO_xH_y$ nanoparticles (NPs) composite as a highly efficient OER electrocatalyst. First, through a facile solvothermal method, the mesoporous $Ni(OH)_2$ @FeOOH nanosheets were synthesized. Following a phosphorization process, the solid composite nanosheets were converted into the mesoporous Ni_2P @ $FePO_xH_y$ NPs composite. The as-synthesized mesopores nanostructure of Ni_2P @ $FePO_xH_y$ catalyst provides abundant exposed active sites and enhanced electrochemical surface area [23,24]. These mesopores also facilitate the adsorption/-desorption process, largely improving the catalytic activity [23,24]. In addition, the unique formation of crystalline (Ni_2P) and amorphous ($FePO_xH_y$) phases in a single structure obtained at low-temperature phosphorization provide more electrocatalytic active sites which we speculate further play a significant role in enhanced electrocatalytic performance [20,21]. The OER electrocatalyst demonstrates impressive OER activities in alkaline media (1 M KOH) with long-term stability. The mesoporous Ni_2P @ $FePO_xH_y$ shows $\eta = 220$, 260, and 360 mV at $j = 10$, 100, and 1000 mA cm^{-2}, respectively. These catalysts' improved electrochemical performances and prolonged stability are well supported by a low charge transfer resistance, mesoporous structure, and the synergistic effect between Ni_2P and $FePO_xH_y$. Hence, the Ni_2P @ $FePO_xH_y$ NPs nanocomposite could utilize the crystalline–amorphous interfaces, where the two phases coexist, designed to improve the OER activity and stability over the individual phases, either crystalline or amorphous [20,21]. The mesoporosity of this Ni_2P @ $FePO_xH_y$ was confirmed by Brunauer–Emmett–Teller (BET) analysis. Along with efficient HER catalyst in a highly corrosive environment (30% KOH) used for commercial water splitting, the catalyst also achieves high $j = 500$ and 1000 mA cm^{-2} at 1.65 and 1.715 V, respectively, with long-term durability. Further, the catalyst delivers $j = 1$ A cm^{-2} at a cell voltage of 1.84 V in a commercial AAEMWE cell working with 1 M KOH, outperforming the commercially used Pt/C–IrO_2 catalyst.

2. Experimental section

2.1. Chemicals

All chemicals of analytical grade were used as received without further purification. Nickel (II) chloride, Iron (III) chloride, 5 wt% of Nafion, potassium hydroxide, sodium hydroxide, and sodium hypophosphite monohydrate were purchased from Sigma Aldrich. Commercial 20 wt% Pt/C was obtained from Johnson Matthey, and iridium oxide powder (IrO_2, 99%) was purchased from Alfa Aesar. All aqueous solutions used during the synthesis were prepared using deionized water (DI). Nickel foam (MTI Corporation) was used as received.

2.2. Synthesis of $Ni(OH)_2$ @FeOOH and Ni_2P @ $FePO_xH_y$ NPs

The mesoporous $Ni(OH)_2$ @FeOOH NPs were synthesized through a simple hydrothermal method. Typically, $FeCl_3$ (0.11 M) and $NiCl_2$ (0.22 M) were dissolved into 120 ml of DI water, and the solution was stirred vigorously for 10 min to form a homogeneous solution. NaOH (2 M) solution in 60 ml of DI water was then added dropwise to the above solution to create a NiFe suspension, which was stirred for 60 min. The obtained $Ni(OH)_2$ @FeOOH suspension was then washed with distilled water and ethanol to remove impurities. Immediately, the $Ni(OH)_2$ @FeOOH suspension without drying was quickly transferred to the aqueous solution of NaOH (2.5 M) in 210 ml of DI water. The aqueous solution was transferred to three 100 ml Teflon-lined stainless-steel autoclaves, which are sealed, maintained at 160 °C for 24 h, and then allowed to cool to room temperature naturally. After the reaction, the Ni $(OH)_2$ @FeOOH NPs were taken out and washed with ethanol and water thoroughly before drying at 60 °C for 8 h. To prepare Ni_2P @ $FePO_xH_y$, first $Ni(OH)_2$ @FeOOH NPs precursor (100 mg) and 1 g $NaPO_2H_2{\cdot}H_2O$ were put on a porcelain boat, separated by a distance of 2–3 cm, with the $NaPO_2H_2{\cdot}H_2O$ on the upstream side and $Ni(OH)_2$ @FeOOH NPs on the downstream side, in a tube furnace. Subsequently, the samples were heated at 350 °C for 2 h in a flow Ar atmosphere. The ramping rate of the furnace was set to 2 °C min^{-1}. For comparison, a series of $Ni(OH)_2$ @FeOOH NPs samples were synthesized according to the method as mentioned above with the Fe:Ni ratios being 1:1, 1: 2, 1: 3, and 1:4.

2.3. Synthesis of Ni_2P @ $Fe_2P_2O_7$

The Ni_2P @ $Fe_2P_2O_7$ was synthesized under a similar method for Ni_2P @ $FePO_xH_y$ preparation. The difference was that the $Ni(OH)_2$ @FeOOH NPs were phosphorized at a higher temperature of 650 °C (2 °C min^{-1}) for 2 h to obtain Ni_2P @ $Fe_2P_2O_7$ NPs.

2.4. Synthesis of Ni_2P

For comparison studies, the Ni_2P NPs were synthesized in the same conditions as Ni_2P @ $FePO_xH_y$ NPs. First, $Ni(OH)_2$ NPs were synthesized in similar conditions as $Ni(OH)_2$ @FeOOH preparation without adding $FeCl_3$ in the initial state. As obtained, $Ni(OH)_2$ NPs were further phosphorized at 600 °C for 2 h in the Ar atmosphere (2 °C min^{-1}) to obtain Ni_2P NPs.

2.5. Synthesis of $MoNi_4/MoO_2$ cuboid arrays

First, we synthesized $NiMoO_4$ cuboid arrays on commercial nickel foam via a hydrothermal procedure previously reported by Zhang et al. [25]. A clean nickel foam was immersed into the as-prepared solution consisting of 34 ml of DI water, $Ni(NO_{3)2}6$ H_2O (0.04 M) and $(NH_4)_6Mo_7O_{24}4$ H_2O (0.01 M) in a 50 ml Teflon autoclave. The autoclave was then placed in a drying oven, which was heated at 150 °C for 6 h. After water cleaning, the $NiMoO_4$ cuboid arrays grown on nickel foam

were obtained and dried in an oven for 8 h before H_2 treatment. The as-obtained $NiMoO_4$ cuboid arrays on nickel foam were placed in a tube furnace in an Ar/H_2 (95 sccm Ar / 5 sccm H_2) atmosphere at 500 °C for 2 h. After cooling to room temperature, the $MoNi_4/MoO_2$ cuboid arrays were obtained.

2.6. Structure characterization

The high-resolution powder X-ray diffraction (HRPXRD) measurements were performed on a RIGAKU (smart lab) X-Ray analysis instrument. The X-ray photoelectron spectroscopy (XPS) data were collected on a Thermo Fisher (K-alpha) instrument. The cold field emission scanning electron microscope (FE-SEM) images were taken using a Hitachi High-Technologies (SU-8220) microscope. High-resolution transmission electron microscopy (HRTEM) images were collected on JEM-2100 F, JEOL, with an acceleration voltage of 200 kV. The surface area and porosity were measured on micromeritics instruments (ASAP2420) system. The electrical conductivity of the samples was measured with a CMT2000N four-point probing system. The weight percentages of elements in the catalyst were determined using ICP-MS (PerkinElmer, ELAN DRC-II) and EA (Flash 2000, Thermo Fisher).

2.7. Electrochemical measurements

All electrochemical tests were performed in a three-electrode system in 1 M and 30% KOH electrolyte solution using an electrochemical VSP instrument (BioLogic Science Instruments, Inc.). A graphitic road and Hg/HgO reference were used as the counter and reference electrodes, respectively. The as-prepared different powder catalysts were loaded directly on nickel foam and were used as the working electrode. First, for drop-casting a catalyst ink was prepared, 5 mg of the catalyst powder was dispersed in a mixture of 50 μL alkaline anion exchange membrane (AAEM) solution, 700 μL of isopropyl alcohol and 250 μL deionized water. After 120 min of sonication, the solution became homogeneous, and from the resultant catalyst ink a total of 4 mg cm^{-2} loading amount of catalyst on nickel foam was achieved, and the sample was dried at 40 ℃. The OER activity of electrocatalysts was measured using the steady-state polarization curve in an oxygen saturated environment. The steady-state polarization curve with 100% manual iR drop compensation was constructed by sampling OER current density at the 100th second of chronoamperometry (CA) responses acquired at various overpotentials in the catalytic turnover region with a regular interval of 0.050 V [12,26,27]. Similarly, the steady state polarization curves were also obtained for overall water splitting [28]. The steady-state polarization curves were manual iR corrected by the equation of $E_{cor} = E_{RHE} - i \times R_s$, where E_{cor} is the corrected potential (V), i is the test current (A), and R_s is the solution resistance obtained from electrochemical impedance spectroscopy (EIS, Ω). In contrast, the electrocatalyst long-term durability was measured by performing chronopotentiometry and cyclic voltammetry (CV) testing in a three-electrode system. All the Hg/HgO electrode potentials were converted to a reversible hydrogen electrode (RHE) according to the following equation (Fig. S16): E(RHE) = E(Hg/HgO) + 0.905. Electrochemical impedance spectra (EIS) of the samples were obtained at 1.53 V (vs. RHE) for OER in the frequency range of 10 kHz − 10 mHz with an AC voltage of 10 mV in 1 M KOH electrolyte. Conventional alkaline water electrolysis cell with a separator type of fine glass frit was tested using the Ni_2P @ $FePO_xH_y$ electrode as an anode and the $MoNi_4/MoO_2$ electrode as a cathode (Ni_2P @ $FePO_xH_y$ −$MoNi_4/MoO_2$) in 1 M and 30% KOH. The distance between anode and cathode is 5 cm. The double-layer capacitance (C_{dl}) measurements were made in a non-Faradic region under different applied scan rates ranging from 10 to 50 mV s^{-1}. The electrochemical surface area (ECSA) was determined by dividing the Cdl with the specific capacitance of the electrode material. The following equation estimated the ECSA:

$$ECSA = C_{dl}/C_s$$

where Cs, the specific capacitance for flat surface electrodes, is 0.04 mF cm^{-2}.

2.7.1. Faradaic efficiency

Faradic efficiency was calculated by the rotating ring disk electrodes (RRDE) in an entirely inert environment (N_2 or Ar saturated), with the polished Pt ring assembled on a glassy carbon disk. The Ni_2P @ $FePO_xH_y$ catalyst was drop-cast on the glassy carbon (GC) disk electrode. The oxygen is produced from the working electrode, which will be reduced by the platinum ring electrode on constant potential. The current produced at the ring depends on produced oxygen molecules concentration, and the faradic efficiency was calculated based on the following equation:

$$\text{Faradaic efficiency} = \frac{2i_r}{i_d N_{CL}}$$

where i_r and I_d represent the ring and disc current, respectively, and N_{CL} is the ring collection efficiency (%) of the RRDE.

2.7.2. Mass activity (j_m, Ag^{-1})

$$j_m = \frac{j_{geo}}{m}$$

Where m is catalyst loading (g) and j_{geo} is geometrical current density (A cm^{-2}) at 1.53 V vs. RHE.

2.7.3. Turnover frequency

The TOF of the Ni_2P @ $FePO_xH_y$ was calculated by using the following equation [29].

$$TOF = \frac{(J \times N_A)}{(4 \times F \times \Gamma)}$$

where J stands for current density (A cm^{-2}), N_A is Avogadro number, F is the Faraday constant, and Γ is the surface concentration of active sites or number of participating atoms in the catalyst material.

2.7.4. Surface concentration of active sites

Surface active concentration of metal sites is integrating the area below the redox peak for the redox reaction of oxide/hydroxide to oxyhydroxide formation (equivalent to the number of redox active Ni atoms). In this method, only the metal sites undergoing in situ oxidation and reduction just before the onset of OER are assumed to be participating in the catalysis of OER. This is reasonable because all OER mechanisms which have been proposed to date in the literature emphasize the in situ oxidation and reduction of the active site in a single complete cycle [29,30].

2.7.5. Membrane pre-treatment for AAEMWE fabrication

Before MEA Fabrication, the Anion Exchange Membrane (Sustainion® X37–50) was pretreated in an alkaline solution (0.5 M KOH) for more than 24 h and afterward washed with DI water membrane was ion-exchanged into a hydroxyl form. Furthermore, the pretreated membrane was stored under a humidified and CO_2-free condition to avoid CO_2 contamination.

2.7.6. AAEMWE Assembly

The catalyst-coated substrate (CCS) method was used for the membrane electrode fabrication [5,31]. 6.0 mg of catalyst (Ni_2P @ $FePO_xH_y$) was dispersed in 110 μL of deionized water, 310 μL of isopropyl alcohol (IPA), and 80 μL of alkaline anion exchange membrane (AAEM) binder solution with the help of sonication (40–60 min) to form a homogeneous ink. The as-prepared catalyst ink was drop cast on the nickel foam and dried at 60 ℃. After that, the catalyst-loaded nickel foam was

compressed (3.5 MPa). The compression of nickel foam reduced the thickness, porosity, and roughness of the foam and also ensured that the catalyst would not be lost during assembly into a single AAEMWE cell [32]. The membrane electrode assembly (MEA) is shown in Fig. 5a. The pretreated membrane was sandwiched between Ni_2P @ $FePO_xH_y$ and $MoNi_4/MoO_2$ electrode as anode and cathode, respectively, followed by hot-pressing (40 °C, 5 MPa) for 1–2 min. Then, the Ni_2P @ $FePO_xH_y$ and $MoNi_4/MoO_2$ electrodes and membrane were assembled into a membrane-electrode assembly (MEA), which was incorporated with other different parts (a stainless-steel endplate, silicone gasket, and Ti gas diffusion layer) into the electrolyzer (Fig. 5a). For comparison studies, the homemade AAEMWE cell hardware was assembled using IrO_2 and 20% Pt/C on the nickel foam with a catalyst loading of 2.5 mg cm^{-2} and 5 mg cm^{-2}, respectively. The active area of the single cell is 2 cm × 2 cm.

2.7.7. Single-cell performance analysis

All electrochemical single-cell measurements were performed using 1 M KOH as an electrolyte at 60°C temperature under ambient pressure. The KOH solution was fed into the cathode side and recirculated with a water circulator pump. The steady-state polarization curves for Ni_2P @ FePOxHy–MoNi4/MoO2 cells were recorded at constant current densities ranging 50–1000 mA cm^{-2} (without iR correction).

3. Results and discussion

3.1. Synthesis and characterization

$Ni(OH)_2$ @FeOOH NPs were first synthesized through a hydrothermal method using different Ni/Fe ratios as a typical synthesis. The X-ray diffraction (XRD) patterns of the $Ni(OH)_2$ @FeOOH NPs match well with the standard patterns of $Ni(OH)_2$ (PDF#00–059–0462) and FeOOH (PDF#01–074–3080) (Fig. 1a). The $Ni(OH)_2$ @FeOOH NPs were phosphorized (350 °C) using $NaH_2PO_2{\cdot}H_2O$ to obtain Ni_2P and P-doped FeOOH NPs(Ni_2P @ $FePO_xH_y$). The XRD measurements further confirmed the formation of Ni_2P and P-doped FeOOH NPs (Ni_2P @ $FePO_xH_y$), which was supported by HRTEM. All characteristic peaks of $Ni(OH)_2$ entirely disappeared after phosphorization by converting into Ni_2P. In contrast, the characteristic peaks of P-doped FeOOH were maintained, but no additional XRD peaks of other phosphorus compounds were observed. To find the suitable phosphorization temperature for the best electrocatalyst, different control experiments were performed, and it was found that the phosphorization temperature played a vital role during the formation of Ni_2P @ $FePO_xH_y$ NPs. As we further increased the phosphorization temperatures from 350 °C to 450 °C, the Ni_2P @ $FePO_xH_y$ structure was maintained (Fig. S1a). However, this composite was fully converted into highly crystalline Ni_2P @ $Fe_2P_2O_7$ above 550 °C; here, $FePO_xH_y$ was converted to $Fe_2P_2O_7$, and the same structure was maintained up to 650 °C (Fig. S1a). Ni_2P @ $FePO_xH_y$ samples with different Fe/Ni ratios were also successfully fabricated. Among all these synthesized samples, the Ni_2P @ $FePO_xH_y$ with a Fe/Ni ratio of 1:2 exhibited the best catalytic activity. Besides, X-ray photoelectron spectroscopy (XPS) was performed to determine if the original material was indeed Ni_2P @ $FePO_xH_y$. The high-resolution Ni 2p spectrum displayed six prominent peaks (Fig. 1b). The peaks located at 853.26, 870.48, 856.98, and 874.82 eV correspond to the Ni $2p_{3/2}$, and Ni $2p_{1/2}$ of Ni-P as well as Ni $2p_{3/2}$ and Ni $2p_{1/2}$ of Ni-O, respectively [33]. The oxidized species associated with nickel oxide and phosphates were ascribed to the surface oxidation of Ni_2P when it was exposed to air. The XPS spectra Fe 2p of Ni_2P @ $FePO_xH_y$ (Fig. 1c) showed two major binding energy peaks with two shake-up satellites (sat.) at 711.77 (Fe $2p_{3/2}$), 725.38 (Fe $2p_{1/2}$),

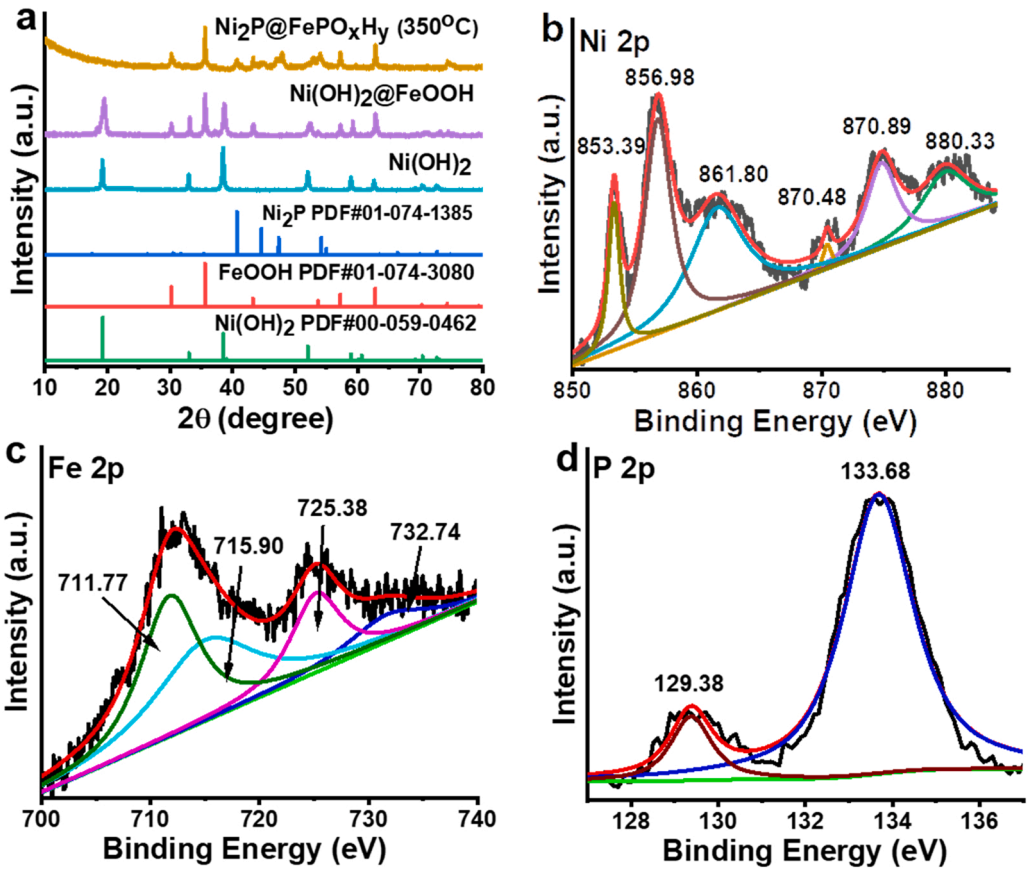

Fig. 1. Structural and compositional characterization of Ni_2P @ $FePO_xH_y$.(a) XRD patterns of as-prepared samples of Ni_2P @ $FePO_xH_y$ and $Ni(OH)_2$ @FeOOH. (b-d) High-resolution XPS spectra for constituent elements: (b) Ni 2p, (c) Fe 2p and (d) P 2p.

715.90 (Fe $2p_{3/2}$ sat.), and 732.74 eV (Fe $2p_{1/2}$sat.), respectively, suggesting that the charge state of Fe was + 3 [34]. Similarly, the high-resolution P 2p spectrum (Fig. 1d) showed the existence of both metal phosphate (133.68 eV) and metal phosphide (129.38 eV) [35]. All the above results confirm the co-existence of metal phosphates species, Fe^{3+}, Ni^{2+}, and Ni_2P.

Field emission scanning electron microscopy (FE-SEM) and high-resolution transmission electron microscopy (HR-TEM) were employed to study the structure of catalysts (Fig. 2 and Figs. S1–4). FE-SEM (Fig. 2a) and TEM (Fig. S1d) images revealed that mesoporous Ni $(OH)_2$ @FeOOH NPs had a hexagonal nanosheet like morphology (Fig. S1b-f). After phosphorization, the nanosheet-like morphology of Ni $(OH)_2$ @FeOOH NPs was destroyed entirely (Fig. 2b). The HRTEM images showed mixed crystalline and amorphous Ni_2P @ $FePO_xH_y$ NPs synthesized at 350 °C (Fig. 2c and Fig. S2a-c). The lattice fringes of the crystalline NPs (Fig. 2c) showed the interplanar spacings (*d*-spacing) of 0.253 and 0.204 nm corresponding to the (200) and (021) planes of Ni_2P NPs [36,37]. These *d*-spacing results further confirmed the formation of crystalline Ni_2P NPs in Ni_2P @ $FePO_xH_y$. The EDS line-scan profiles (Fig. 2d-e) across crystalline to the amorphous phase of Ni_2P @ $FePO_xH_y$ showed that Ni and P intensities were in the crystalline region compared to Fe and O (Fig. 2f). However, in the amorphous zone, the intensities of Fe and O started to increase while Ni started to decrease, indicating that the crystalline and amorphous zones corresponded to Ni_2P and $FePO_xH_y$, respectively (Fig. 2d-f). The energy-dispersive X-ray spectroscopy (EDS) elemental mapping images (Fig. 2g and Fig. S2d) of Ni_2P @ $FePO_xH_y$ NPs demonstrated that the Ni element was evenly distributed in the crystalline Ni_2P NPs. In contrast, the Fe and O elements were primarily dispersed in the amorphous NPs. Additionally, the P element was uniformly distributed over the Ni_2P @ $FePO_xH_y$ NPs. Both the line scan and EDS results confirmed that the crystalline NPs primarily consisted of Ni_2P, and the amorphous substrate part was most likely to be $FePO_xH_y$ NPs. The formation of crystalline Ni_2P NPs suggested that $Ni(OH)_2$ was selectively phosphorized and extracted from $Ni(OH)_2$ @FeOOH during the phosphorization because the Ni^{2+} in $Ni(OH)_2$ could be easily phosphorized by substituting the O atoms with P atoms to form Ni_2P. The iron oxyhydroxide (FeOOH) was transformed to iron phosphate rather than iron phosphide due to the high affinity of Fe^{3+} towards oxygen, which further hampered the substitution of O atoms by P atoms [38,39]. The specific surface area and pore size distribution of Ni_2P @ $FePO_xH_y$ were studied using the N_2 adsorption and desorption isotherms. The BET surface area of Ni_2P @ $FePO_xH_y$ is 17.50 m^2g^{-1}, and the pore size distribution determined by the Barrett–Joyner–Halenda (BJH) method showed a narrow peak with a mean value of 31.1 nm (Fig. S5). The electrocatalyst with mesoporous structure usually exhibited high catalytic activity because of more exposed active sites [23,24]. The BET surface area of $Ni(OH)_2$ @FeOOH is 36.34 m^2g^{-1}.

3.2. OER activity of Ni_2P @ $FePO_xH_y$ electrocatalyst

The electrocatalytic activity of Ni_2P @ $FePO_xH_y$ was investigated using linear-sweep-voltammetry (LSV) in a standard three-electrode system in the O_2 saturated 1 M KOH electrolyte. The Ni_2P @ $FePO_xH_y$ catalyst shows Ni oxidation peaks located in the potential range of 1.3–1.5 V (vs. RHE), before the OER process, for which the oxidation of Ni ranges from low valence states (Ni^0, Ni^{2+}) to high valence states (Ni^{3+} or Ni^{4+}) (Fig. S6a). The higher valence states are considered to be the active sites for OER [14,40]. After Fe incorporation, the positive shift of

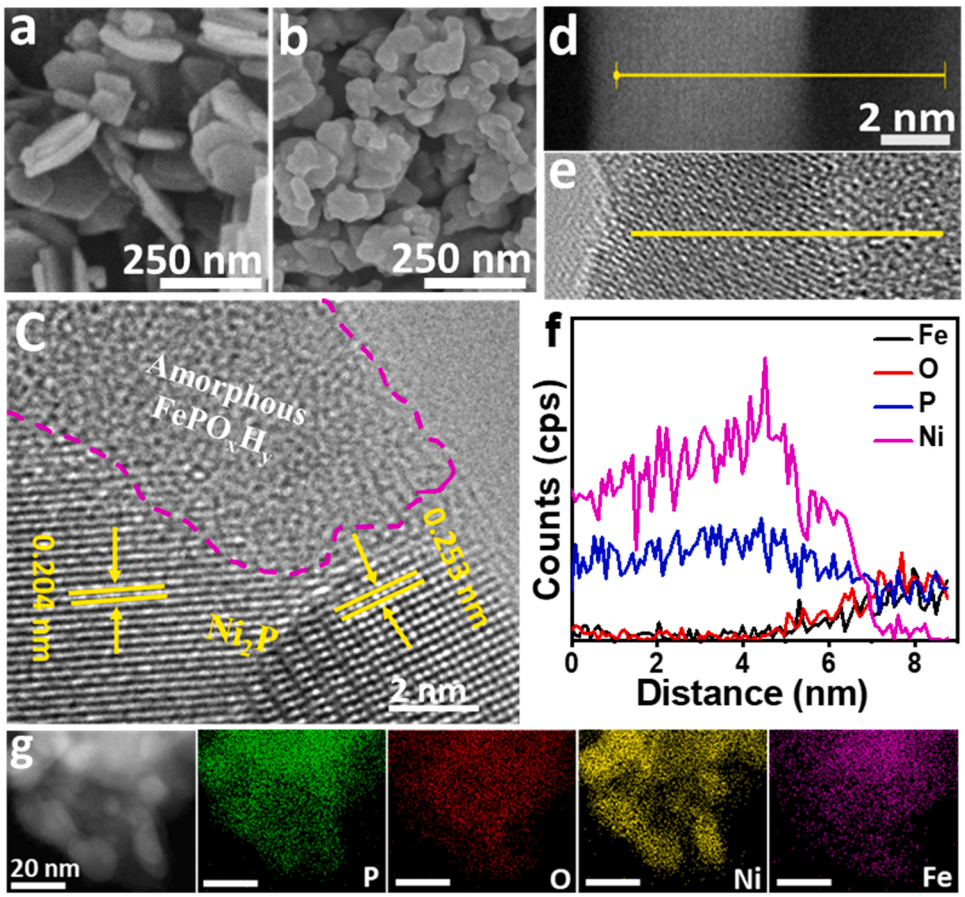

Fig. 2. Morphology and chemical composition analysis Ni_2P @ $FePO_xH_y$. (a, b) FE-SEM images of the as-prepared $Ni(OH)_2$ @FeOOH and Ni_2P @ $FePO_xH_y$, respectively. (c) HRTEM image of Ni_2P @ $FePO_xH_y$. (d, e) Atomic-resolution HAADF-STEM and corresponding HR-TEM images of Ni_2P @ $FePO_xH_y$. (f) Intensity profiles were recorded from the lines shown in panels (d, e). (g) HAADF-STEM image and EDS elemental mapping images.

this redox potential indicates alteration of the redox properties of Ni in Ni_2P @ $FePO_xH_y$, and such synergistic interaction between Ni_2P and $FePO_xH_y$ results in enhanced oxygen evolution (Fig. S6a). This phenomenon of the positive shift of nickel redox potential after iron incorporation was reported previously [41–43]. The steady-state polarization curve was constructed to evaluate the true OER activity and Tafel slope [26,44,45]. The electrocatalytic activity of Ni_2P @ $FePO_xH_y$ was investigated using the steady-state polarization curve constructed chronoamperometry responses in a standard three-electrode system in the O_2 saturated 1 M KOH electrolyte solution. Representative steady-state polarization curve in Fig. 3a shows the j plotted against applied potential vs. reversible hydrogen electrode (RHE) of Ni_2P @ $FePO_xH_y$ NPs electrode, and the OER performance of $Ni(OH)_2$ @FeOOH, Ni_2P @ $Fe_2P_2O_7$, Ni_2P, and benchmark IrO_2 catalysts on nickel foam were also tested under the same condition for comparison. The steady-state polarization curve in Fig. 3a shows that the Ni_2P @ $FePO_xH_y$ NPs electrode exhibits the best OER performance, with higher current density and lower overpotential.Strikingly, Ni_2P @ FePOxHy catalyst requires a small $\eta = 220$ mV to deliver 10 mA cm− 2, which is much lower than Ni_2P (300 mV), confirms the synergistic effect by Fe incorporation (Fig. 3a). The combined effect of materials (Ni/Fe) is much superior to the sum of each material given alone (Ni or Fe), and this effect is also known as the synergistic effect. The introduction of Fe in the Ni_2P @ $FePO_xH_y$ catalyst leads to more accessible active metal sites and an improved electron-rich environment, both of which are highly advantageous to promote OER activity [30,46–48]. The η value of Ni_2P @ $FePO_xH_y$ is also much lower compared with those of $Ni(OH)_2$ @FeOOH (274 mV), Ni_2P @ $Fe_2P_2O_7$ (227 mV), and benchmark IrO_2 (269 mV), indicating that the OER catalytic activity is enhanced after the formation of Ni_2P @ $FePO_xH_y$ NPs. What is more important is that it only required low $\eta = 260$ and 360 mV to achieve $j = 100$ and 1000 mA cm^{-2}, respectively. Besides, we measured a minimal Tafel slope of 43 mV dec^{-1} for Ni_2P @ $FePO_xH_y$ catalyst (Fig. 3b), which is much smaller than those of the reference materials Ni_2P (55 mV dec^{-1}), and $Ni(OH)_2$ @FeOOH (52 mV dec^{-1}), suggesting its fast catalytic rate and favorable OER kinetics. We performed electrochemical impedance spectroscopy (EIS) and double-layer capacitance (Cdl) examinations on this Ni_2P @ FePOxHy electrode to determine the possible origins of such remarkably high OER performance.

The catalyst's enlarged electrochemically active surface area (ECSA) plays a vital role in boosting OER electrocatalyst catalytic performance. To make sure this point, the capacitance C_{dl} determined by a simple CV method was introduced, which is proportional to the catalyst active surface area (Fig. S7a-h). By comparing the C_{dl} values among different catalysts, we found that the Ni_2P @ $FePO_xH_y$ catalyst had a capacitance of 0.48 mF cm^{-2}, very close to those of $Ni(OH)_2$ @FeOOH (0.44 mF cm^{-2}) and Ni_2P (0.433 mF cm^{-2}). The C_{dl} values demonstrated that phosphorization of $Ni(OH)_2$ @FeOOH did not significantly change the active surface area, but the OER performance of Ni_2P @ $FePO_xH_y$ was much better than $Ni(OH)_2$ @FeOOH, Ni_2P @ $Fe_2P_2O_7$, and Ni_2P. Furthermore, from the ECSA normalized current densities of catalyst shown in Fig. S7i, the Ni_2P @ $FePO_xH_y$ composite required moderate $\eta = 265$ mV to deliver 10 mA cm^{-2}, smaller than those of $Ni(OH)_2$ @FeOOH (337 mV), Ni_2P @ $Fe_2P_2O_7$ (279 mV), and Ni_2P (361 mV). From here, we conclude that the synergistic effect between Ni_2P and $FePO_xH_y$ in the composite is the main factor in our superior catalytic activity, not the ECSA. Meanwhile, we also performed EIS measurements to find out the electrode kinetics of different catalysts. EIS spectra showed that this Ni_2P @ $FePO_xH_y$ composite had a smaller charge-transfer resistance, suggesting its high electronic conductivity and fast charge transfer kinetics at the electrode-electrolyte interface during the OER (Fig. 3c). Additionally, their specific electrocatalytic activities were also obtained by normalizing the measured currents with respect to their BET surface areas before and after phosphorization (Fig. S8a). Their specific electrocatalytic activities exhibited almost the same trend with their geometric area and ECSA normalized electrocatalytic activities. Consistently, the intrinsic electrical conductivity/ resistance of the as-prepared materials in Fig. S8b,c confirmed the above results. Besides, the intrinsic OER activity of as-synthesized nanoparticles was investigated. The mass activity and turnover frequency (TOF) was calculated at an $\eta = 300$ mV (Fig. 3d) [29,49]. The TOF of Ni_2P @ $FePO_xH_y$ catalyst (1.45×10^{-4} s^{-1}) was higher than that of Ni_2P @ $Fe_2P_2O_7$ (6.6×10^{-4} s^{-1}), and $Ni(OH)_2$ @FeOOH (2.97×10^{-5} s^{-1}). We achieved a mass

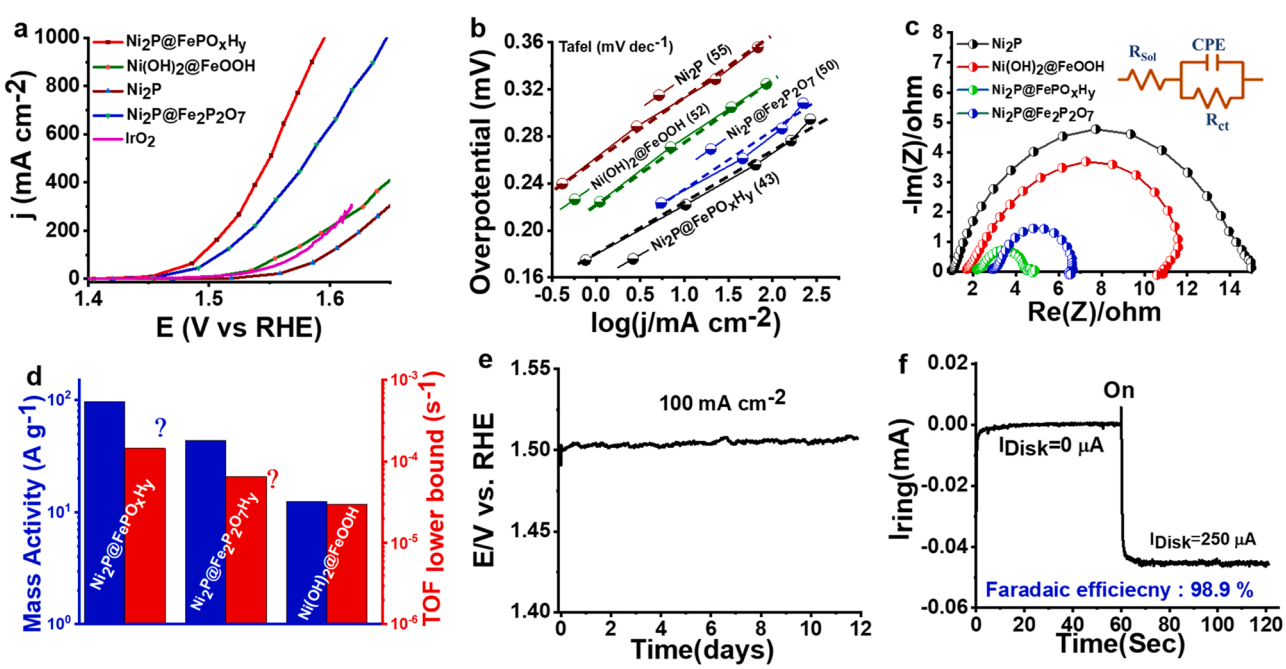

Fig. 3. Oxygen evolution performances of Ni_2P @ $FePO_xH_y$. (a) The steady-state polarization curve was constructed from current sampled from CA responses. (b) Tafel slopes. (c) Electrochemical impedance spectroscopy (EIS). (d) Mass activity and TOF of the catalysts (at $\eta = 300$ mV). (e) Long-term stability test performed at a constant $j = 100$ mA cm^{-2}. (f) Faradaic efficiency measurement; curves were obtained from RRDE.

activity of 96.25 Ag^{-1} with Ni_2P @ $FePO_xH_y$, 7.7 fold higher than Ni $(OH)_2$ @FeOOH, revealing the excellent OER activity of Ni_2P @ $FePO_xH_y$ (Fig. 3d). Table S1 provides the summary data of different critical information.

Furthermore, the catalytic OER performances were compared by changing the Fe/Ni ratio in Ni_2P @ $FePO_xH_y$ catalyst and phosphorization temperature. Fe/Ni in the ratio of 1:2 with 4 mg catalyst loading showed the best catalytic activity compared to other catalyst ratios in Ni_2P @ $FePO_xH_y$ (Fig. S6b-c). The Ni_2P catalyst alone without Fe incorporation did not show high OER activity. Once the amorphous $FePO_xH_y$ composite with crystalline Ni_2P was formed (350 °C), the performance was highly improved, which was better than the fully crystalline Ni_2P @ $Fe_2P_2O_7$ (650 °C) composite (Fig. S8d). These OER comparisons confirm the strong synergistic effect between Ni/Fe and crystalline-amorphous interphase in Ni_2P @ $FePO_xH_y$ composite [14,20,21]. Compared to the pure crystalline composite, the amorphous phase of $FePO_xH_y$ having a higher number of randomly-oriented bonds with unsaturated electronic arrangements promoted the adsorption of reactants. Meanwhile, the crystalline phase of Ni_2P could facilitate electron transfers to the adsorbed reactants, which we speculate would improve the catalytic activity of the composite [20,21,50]. Consistently, the EIS (Fig. 3c) and electrical conductivity/resistance (Fig. S8b,c) measurements confirm the conductivity of metal phosphides, which is higher than oxides. Primarily, oxidized species ($FePO_xH_y$) with Ni_2P in Ni_2P @ $FePO_xH_y$ play a critical role in superior OER activity, according to many recent studies [50]. The $FePO_xH_y$ shows different coordination modes during the redox switching process and helps improve the OER activity [50,51]. The formation of Ni_2P-$FePO_xH_y$ oxide interface (metal phosphide–metal-oxide interface) is beneficial to the adequate carrier transportation from the phosphide core to the oxidized species [50–52]. Considering all the above results, we conclude that the excellent OER performance of our Ni_2P-$FePO_xH_y$ catalyst is attributed to the presence of a sufficient number of amorphous-crystalline sites, mesoporous structure, and synergistic effects between Ni_2P and $FePO_xH_y$.

Electrochemical long-term stability is another critical criterion to evaluate the OER performance of electrocatalysts. As shown in Fig. S8e, after 10,000 cycling tests, the LSV curve of this Ni_2P @ $FePO_xH_y$ composite is nearly identical to the initial one, suggesting its superb stability during cycling scans. We also assessed the catalytic stability of Ni_2P @ $FePO_xH_y$. The chronopotentiometry curves were recorded at 100 mA cm^{-2} in 1 M KOH solution, finding that the potential remained nearly constant for more than 12 days (288 h), with minimal potential loss rates (only 0.02 mV h^{-1}). The stability test further confirms the long-term durability of Ni_2P @ $FePO_xH_y$ catalyst for OER. After such long-time electrocatalysis stability tests, further insights into the chemical compositions for post OER samples by XPS, SEM, and HR-PXRD confirm a mixture of nickel and iron oxides/oxyhydroxides formed during the OER test in the alkaline environment (Fig. S9-12). After the cyclic stability tests, FE-SEM and elemental mapping images (Fig. S9b-d) of the generated sample indicate no apparent change in Ni_2P @ FePOxHy nanoparticle morphology. As shown in the XRD pattern (Fig. S9a), the characteristic diffraction peaks of Ni_2P and FeOOH were detected. The peaks assigned to Ni_2P showed a decrease in intensity compared to the initial Ni_2P @ $FePO_xH_y$ catalyst, while some new peaks attributed to nickel oxides/oxyhydroxides appeared after the OER test. However, the XPS analysis showed the disappearance of the low-energy characteristic peaks of 129.38 and 853.39 eV belonging to Ni_2P in Ni_2P @ $FePO_xH_y$ after cyclic stability tests (Fig. S10). This suggests the surface oxidation of Ni_2P to form nickel oxides/oxyhydroxides during OER [38,53,54]. The XPS spectrum (Fig. S10c) of the P element whose peak at 133.68 eV decreased significantly after the stability taste confirms that $FePO_xH_y$ was not entirely oxidized to form iron oxides/oxyhydroxides. A small amount of $FePO_xH_y$ was still left. HRTEM (Fig. S11a-b) images of the generated sample indicate the amorphous iron phosphate was transformed into crystalline FeOOH in 1.0 M KOH, which was also confirmed by XRD measurement (Fig. S9a). Ni_2P @ $FePO_xH_y$ after long-term stability test performed at a constant j = 100 mA cm^{-2} in 1 M KOH further confirm the complete surface oxidation of Ni_2P and $FePO_xH_y$ to form nickel and iron oxides/oxyhydroxides during OER (Fig. S12). The XPS spectrum (Fig. S12d) of the P element in Ni_2P @ $FePO_xH_y$ does not show any P characteristic peaks, which confirms the complete oxidation FePOxHy to form iron oxide/oxyhydroxides. HRTEM images (Fig. S12f) of the generated sample further confirm the formation of nickel and iron oxides/oxyhydroxides. The FE-SEM EDS elemental analysis (Fig. S13b and Table S2) also confirms the instability of phosphorous during the long stability tests. These observations indicate that the Ni and Fe oxides/oxyhydroxides formed on the surface of Ni_2P @ $FePO_xH_y$ catalyst during the OER enhanced the active catalytic sites for the OER catalysis [50,53,55]. Furthermore, the physical stability of Ni_2P @ $FePO_xH_y$ was also confirmed with inductively coupled ICP-MS measurement of Ni and Fe in the electrolyte (Fig. S13a and Table S3) after a 12 days constant current electrolysis at a constant j = 100 mA cm^{-2}. As shown in Table S3, after 12 days of electrolysis, trace amounts of Fe (0.576 mg L^{-1}) and Ni (0.691 mgL^{-1}) were detected in the electrolyte, which correspond to only 6.5 wt% of Fe and 4.4 wt% of Ni in the fresh electrode.

It is suggested that metal phosphides and phosphates-based electrocatalysts are not stable under practical alkaline OER conditions. They typically transform into metal oxides/oxyhydroxides during the OER process because of the leaching of the phosphorus [42,50]. The phosphorus leaching further results in the structural reorganization, increased surface area, and roughening, as smaller oxides/oxyhydroxides anions commonly replace the larger phosphorus anion [56–58]. The increased surface area from the new porous structures arising from phosphorous leaching results in a higher number of active sites for the enhanced OER performance. The Ni_2P @ $FePO_xH_y$ catalyst, after long--time electrocatalysis stability tests, converted into nickel and iron oxides/oxyhydroxides. However, it still showed better performance than native metal oxides/oxyhydroxides ($Ni(OH)_2$ @FeOOH) because of better surface roughness and the higher number of active sites [58]. Faradaic efficiency from rotating ring-disk electrodes (RRDE) was also calculated for Ni_2P @ $FePO_xH_y$ to determine the efficiency of a catalyst to transfer electrons provided by the external circuit, showing that the as-prepared catalyst has an efficiency of ~98.9%, according to Fig. 3f.

3.3. OER activity of Ni_2P @ $FePO_xH_y$ electrode as a conventional alkaline water electrolysis cell

First, a robust $MoNi_4/MoO_2$ cuboid array was prepared as a non-noble metal-based HER electrocatalyst to make a conventional alkaline electrolyzer in 1 M KOH (Fig. S14) [25]. A water electrolysis cell was tested using the Ni_2P @ $FePO_xH_y$ electrode as the anode and $MoNi_4/MoO_2$ electrode as the cathode (Ni_2P @ $FePO_xH_y$ −$MoNi_4/MoO_2$) in 1 M KOH (Fig. 4a) [25]. Surprisingly, the full water-splitting activity of this cell is superior to the commercial Pt/C–IrO_2 on nickel foam. Ni_2P @ $FePO_xH_y$ −$MoNi_4/MoO_2$ electrolyzer at room temperature delivers a cell voltage of 1.491 V to achieve a water-splitting j = 10 mA $cm^{-2,}$ which is substantially lower than that of the commercial benchmarking Pt/C–IrO_2 electrolyzers (1.574 V) (Fig. 4b and Fig. S14e). This OER performance is superior to most recently reported full water splitting cells, which usually need cell voltages higher than 1.50 V to deliver a minimum j = 10 mA cm^{-2} (Fig. 4d and Table S4). Most importantly, our water-electrolyzer produces current densities of 100 and 500 cm^{-2} at cell voltages of 1.58 and 1.724, respectively. Impressively, this performance is superior to Pt/C–IrO_2 electrolyzer at the j = 100 and 500 mA cm^{-2} (Fig. 4b). In contrast, even at 1.7 V cell voltage, most of the previously reported electrolyzers cell delivered j < 142 mA cm^{-2} (Fig. 4e and Table S4). The polarized curves Pt/C–IrO_2 in Fig. 4c show the oxidation peaks at 1.30–1.45 V, which correspond to the oxidation of Ni^{2+} to Ni^{3+} in NF substrate. Electrochemical long-term stability for overall water splitting is an essential metric for catalytic properties. As for the long-term

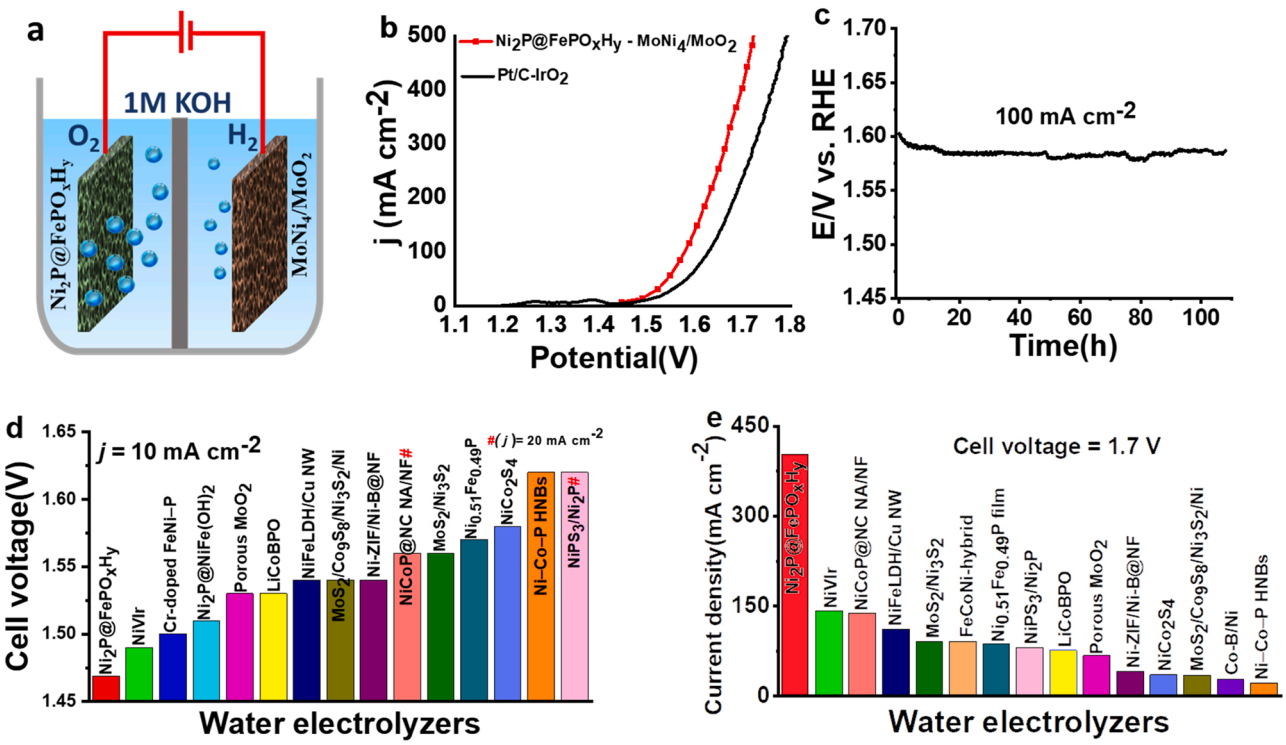

Fig. 4. Overall water splitting activity of Ni_2P @ $FePO_xH_y$ and Pt/C–IrO_2 electrocatalysts in 1 M KOH. (a) Schematic diagram of two-electrode water splitting by a conventional alkaline water-electrolyzer. (b) The steady-state polarization curve constructed with the currents from CA responses of the Ni_2P @ $FePO_xH_y$–$MoNi_4$/MoO_2 coupled catalyst in a two-electrode configuration in 1 M KOH compared with the standard LSV curve of Pt/C-IrO_2 catalyst. (c) Long-term stability test (100 h) performed at constant j = 100 mA cm^{-2}. (d) Comparison of the cell voltages to achieve 10 mA cm^{-2} among different water alkaline electrolyzers (Table S4). (e) Comparison of the current densities at 1.7 V between Ni_2P @ $FePO_xH_y$ and available robust electrolyzers (Table S4).

stability studies, Ni_2P @ $FePO_xH_y$ −$MoNi_4$/MoO_2 electrolyzer sustains a full water-splitting activity remarkably with minor decay for more than 108 h when operating at constant j = 100 mA cm^{-2} (Fig. 4c), with the nominal voltage loss rate of only ~0.06 mV h^{-1}.

Finally, we analyzed the electrocatalytic performances of the Ni_2P @ $FePO_xH_y$ catalyst under extreme vigorous conditions such as concentrated alkaline solution (30% KOH), which is often required in commercial alkaline water electrolysis [59,60]. The OER polarization curve of Ni_2P @ $FePO_xH_y$ in 30% KOH shows low η = 246 and 270 mV to achieve current densities of 500 and 1000 mA cm^{-2}, respectively (Fig. S15a). These results fully satisfy the requirements of commercial water electrolysis (for example, ≥500 mA cm^{-2} at η ≤ 300 mV). Furthermore, the long-term durability of Ni_2P @ $FePO_xH_y$ in 30% KOH was also confirmed. This catalyst shows remarkable stability sustaining its outstanding OER performance for more than 100 h when operated at a constant j = 100 mA cm^{-2} (Fig. S15b) with a negligible voltage loss of only 0.210 mV h^{-1}. These results further indicated that Ni_2P @ $FePO_xH_y$ is catalytically highly stable, active, and mechanically robust. As a proof of concept toward industrial applications, it is necessary to investigate Ni_2P @ $FePO_xH_y$ for the alkaline water electrolysis cell in 30% KOH. This fabricated cell delivered the overall water splitting with a catalytic j = 10 mA cm^{-2} at a low voltage of 1.485 V and generated industrially required j = 100, 500, and 1000 mA cm^{-2} at only 1.557, 1.65, and 1.715 V at room temperature, respectively (Fig. S15c). The Ni_2P @ $FePO_xH_y$ −$MoNi_4$/MoO_2 cell was very stable during whole water splitting for more than 56 h when operated at constant large current densities of 100 mA cm^{-2} in 30% KOH (Fig. S15d), with minimal voltage loss of only 0.192 mV h^{-1}. Overall, these full water splitting results in 1 M and 30% KOH imply that our Ni_2P @ $FePO_xH_y$ electrocatalyst has excellent potential for commercial hydrogen production with high productivity and low cost.

3.4. OER activity of Ni_2P @ $FePO_xH_y$ in Commercial AAEMWE cell

To utilize non-noble metal-based oxides for commercial H_2 production, we developed a proto-type AAEMWE cell mainly to replace high-cost PEM water electrolysis (Fig. 5a). We demonstrated our Ni_2P @ $FePO_xH_y$ electrocatalyst commercial viability in 1 M KOH, consisting of a commercial anion exchange membrane (Sustainion® X37–50) as a separator. The Ni_2P @ $FePO_xH_y$ and $MoNi_4$/MoO_2 electrodes were used as anode and cathode, respectively, in 1 M KOH as an electrolyte at 60 °C (Fig. 5b). The Ni_2P @ $FePO_xH_y$ −$MoNi_4$/MoO_2 electrolyzer cell delivered high j = 1 A cm^{-2} at a cell voltage of 1.84 V, which is far better than commercially used Pt/C−IrO_x catalysts (j = 460 mA cm^{-2} at 1.84 V) in 1 M KOH. The Ni_2P @ $FePO_xH_y$ −$MoNi_4$/MoO_2 AAEMWE cell stability was tested by applying a constant voltage (Fig. 5c and Fig. S18). During the long-term durability test, the AAEMWE cell displayed a constant j = 480 mA cm^{-2} of 1.75 V for 72 h, without any performance degradation. This demonstration could encourage a new focus on water electrolysis toward more commercial applications.

4. Conclusion

A unique, robust, and durable mesoporous Ni_2P @ $FePO_xH_y$ OER pre-catalyst with an abundant crystalline-amorphous interface was successfully synthesized. This OER catalyst only required an η = 360 mV to yield a high j = 1000 mA cm^{-2} in 1 M KOH with excellent long-term stability for 10,000 cycles during OER testing and survive at 100 mA cm^{-2} operation for more than 12 days. The excellent OER activity is attributed to rich metal phosphide–metal oxide and crystalline–amorphous interfaces with mesoporous structure, resulting in more active sites and accessible surface area with fast charge transfer and mass diffusion. Besides, by coupling Ni_2P @ $FePO_xH_y$ with another

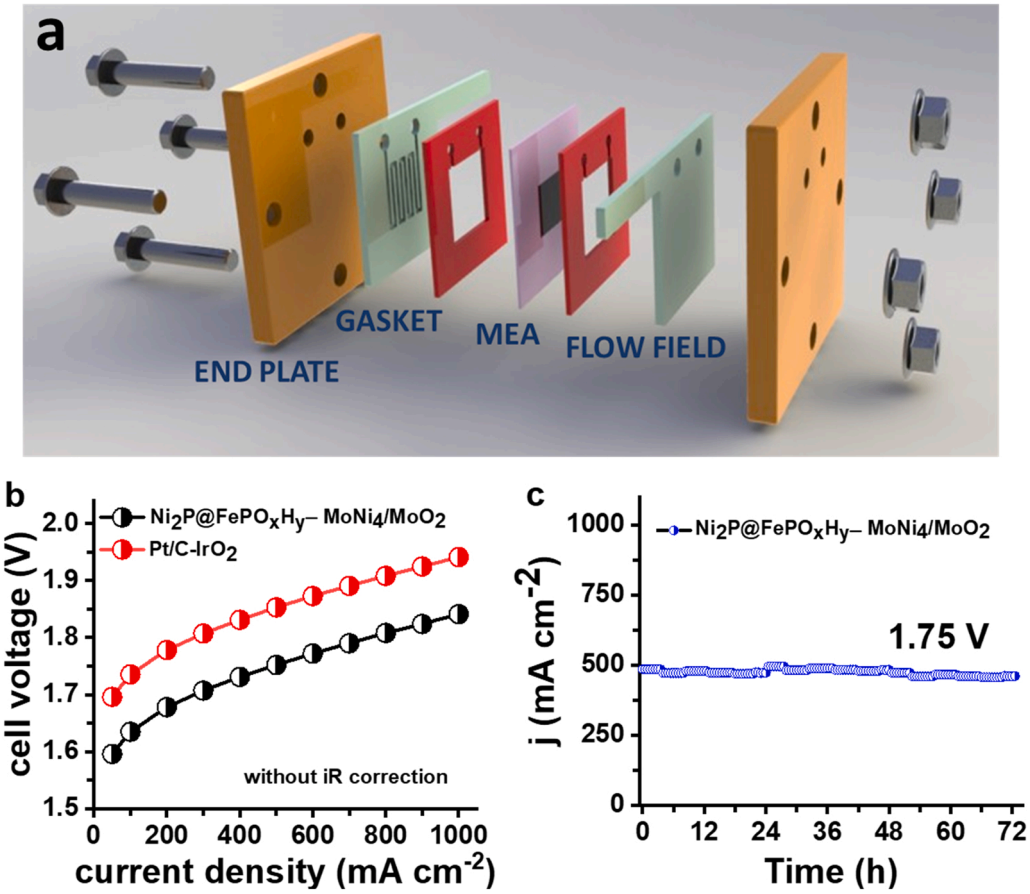

Fig. 5. Overall-water-splitting activity of the Ni_2P @ $FePO_xH_y$–$MoNi_4/MoO_2$ proto-type AAEMWE electrolyzer. (a) Schematic of AAEMWE water-splitting device. (b) The steady-state polarization curves of Ni_2P @ $FePO_xH_y$–$MoNi_4/MoO_2$ vs. Pt/C-IrO_2 in 1 M KOH. (c) Long-term chronoamperometry curve at a fixed operating voltage of 1.75 V for water-splitting in 1 M KOH for an AAEMWE cell.

efficient non-noble HER catalyst in the highly corrosive environment required for industrial application, an outstanding alkaline water-electrolyzer was demonstrated with low voltages of 1.65 and 1.715 V for commercially required j = 500 and 1000 mA cm^{-2}, respectively, for full water splitting in 30% KOH. Furthermore, the extraordinary Ni_2P @ $FePO_xH_y$ catalytic activity in AAEMWWE confirms its commercial application for large-scale hydrogen production. The synthesis process for such a robust electrocatalyst is economically viable and highly suitable for industrially required standards. We believe this work would open new avenues for low-cost, efficient, and economical hydrogen production by water splitting.

CRediT authorship contribution statement

Abhishek Meena: Conceptualization, Validation, Investigation, Writing – original draft, Data curation, Writing – review & editing, Visualization. **Pandiarajan Thangavel:** Validation, Investigation, Data curation, Writing – review & editing, (RRDE experiments, all commercial electrode measurements, and AEM electrolyzer design, fabrication, testing and data analysis). **Da Sol Jeong:** Formal analysis, Validation, Data curation. **Aditya Narayan Singh:** Formal analysis, Validation, Writing – original draft. **Atanu Jana:** Formal analysis, Validation. **Hyunsik Im:** Validation, Data curation. **Duc Anh Nguyen:** Formal analysis, Data curation. **Kwang S. Kim:** Writing – review & editing, Supervision, Project administration, Funding acquisition.

Declaration of Competing Interest

The authors declare that they have no known competing financial interests or personal relationships that could have appeared to influence the work reported in this paper.

Acknowledgments

This work was supported by Basic Science Research Program through the National Research Foundation of Korea (NRF) funded by the Ministry of Education (2021R1I1A1A01050280). A.M. & P.T. thank Dr. M. Thirunavukarasu for helping in designing the schematic of the AAEMWE water-splitting device.

Appendix A. Supporting information

Supplementary data associated with this article can be found in the online version at doi:10.1016/j.apcatb.2022.121127.

References

[1] Y. Jiao, Y. Zheng, M. Jaroniec, S.Z. Qiao, Design of electrocatalysts for oxygen-and hydrogen-involving energy conversion reactions, Chem. Soc. Rev. 44 (2015) 2060–2086.
[2] J.N. Tiwari, S. Sultan, C.W. Myung, T. Yoon, N. Li, M. Ha, A.M. Harzandi, H. J. Park, D.Y. Kim, S.S. Chandrasekaran, W.G. Lee, V. Vij, H. Kang, T.J. Shin, H. S. Shin, G. Lee, Z. Lee, K.S. Kim, Multicomponent electrocatalyst with ultralow Pt loading and high hydrogen evolution activity, Nat. Energy 3 (2018) 773–782.
[3] K. Zeng, D. Zhang, Recent progress in alkaline water electrolysis for hydrogen production and applications, Prog. Energy Combust. Sci. 36 (2010) 307–326.
[4] M. Carmo, D.L. Fritz, J. Mergel, D. Stolten, A comprehensive review on PEM water electrolysis, Int. J. Hydrog. Energy 38 (2013) 4901–4934.
[5] P. Thangavel, M. Ha, S. Kumaraguru, A. Meena, A.N. Singh, A.M. Harzandi, K. S. Kim, Graphene-nanoplatelets-supported NiFe-MOF: high-efficiency and ultra-

stable oxygen electrodes for sustained alkaline anion exchange membrane water electrolysis, Energy Environ. Sci. 13 (2020) 3447–3458.
[6] E. López-Fernández, J. Gil-Rostra, J.P. Espinós, A.R. González-Elipe, A. de Lucas Consuegra, F. Yubero, Chemistry and electrocatalytic activity of nanostructured nickel electrodes for water electrolysis, ACS Catal. 10 (2020) 6159–6170.
[7] F. Lyu, Q. Wang, S.M. Choi, Y. Yin, Noble-metal-free electrocatalysts for oxygen evolution, Small 15 (2019), 1804201.
[8] L. Trotochaud, S.W. Boettcher, Precise oxygen evolution catalysts: status and opportunities, Scr. Mater. 74 (2014) 25–32.
[9] X. Lu, C. Zhao, Electrodeposition of hierarchically structured three-dimensional nickel–iron electrodes for efficient oxygen evolution at high current densities, Nat. Commun. 6 (2015) 6616.
[10] A. Meena, M. Ha, S.S. Chandrasekaran, S. Sultan, P. Thangavel, A.M. Harzandi, B. Singh, J.N. Tiwari, K.S. Kim, Pt-like hydrogen evolution on a V 2 O 5/Ni (OH) 2 Electrocatalyst, J. Mater. Chem. A 7 (2019) 15794–15800.
[11] Y. Li, B. Wei, Z. Yu, O. Bondarchuk, A. Araujo, I. Amorim, N. Zhang, J. Xu, I. C. Neves, L. Liu, Bifunctional porous cobalt phosphide foam for high-current-density alkaline water electrolysis with 4000-h long stability, ACS Sustain. Chem. Eng. 8 (2020) 10193–10200.
[12] L. Wu, J.P. Hofmann, Comparing the intrinsic HER activity of transition metal dichalcogenides: pitfalls and suggestions, ACS Energy Lett. 6 (2021) 2619–2625.
[13] Are Metal Chalcogenides, Nitrides, and Phosphides Oxygen Evolution Catalysts or Bifunctional Catalysts?, ACS Energy Lett., 2, 2017, pp. 1937–1938.
[14] L. Trotochaud, S.L. Young, J.K. Ranney, S.W. Boettcher, Nickel–iron oxyhydroxide oxygen-evolution electrocatalysts: the role of intentional and incidental iron incorporation, J. Am. Chem. Soc. 136 (2014) 6744–6753.
[15] M. Jiang, J. Li, J. Li, Y. Zhao, L. Pan, Q. Cao, D. Wang, Y. Du, Two-dimensional bimetallic phosphide ultrathin nanosheets as non-noble electrocatalysts for a highly efficient oxygen evolution reaction, Nanoscale 11 (2019) 9654–9660.
[16] J. Xu, Y. Liu, J. Li, I. Amorim, B. Zhang, D. Xiong, N. Zhang, S.M. Thalluri, J.P. S. Sousa, L. Liu, Hollow cobalt phosphide octahedral pre-catalysts with exceptionally high intrinsic catalytic activity for electro-oxidation of water and methanol, J. Mater. Chem. A 6 (2018) 20646–20652.
[17] G. Zhang, G. Wang, Y. Liu, H. Liu, J. Qu, J. Li, Highly active and stable catalysts of phytic acid-derivative transition metal phosphides for full water splitting, J. Am. Chem. Soc. 138 (2016) 14686–14693.
[18] J. Xu, J. Li, D. Xiong, B. Zhang, Y. Liu, K.-H. Wu, I. Amorim, W. Li, L. Liu, Trends in activity for the oxygen evolution reaction on transition metal (M = Fe, Co, Ni) phosphide pre-catalysts, Chem. Sci. 9 (2018) 3470–3476.
[19] M. Yao, H. Hu, B. Sun, N. Wang, W. Hu, S. Komarneni, Self-supportive mesoporous Ni/Co/Fe phosphosulfide nanorods derived from novel hydrothermal electrodeposition as a highly efficient electrocatalyst for overall water splitting, Small 15 (2019), 1905201.
[20] H. Han, H. Choi, S. Mhin, Y.-R. Hong, K.M. Kim, J. Kwon, G. Ali, K.Y. Chung, M. Je, H.N. Umh, D.-H. Lim, K. Davey, S.-Z. Qiao, U. Paik, T. Song, Advantageous crystalline–amorphous phase boundary for enhanced electrochemical water oxidation, Energy Environ. Sci. 12 (2019) 2443–2454.
[21] H. Xu, B. Fei, G. Cai, Y. Ha, J. Liu, H. Jia, J. Zhang, M. Liu, R. Wu, Boronization-induced ultrathin 2D nanosheets with abundant crystalline–amorphous phase boundary supported on nickel foam toward efficient water splitting, Adv. Energy Mater. 10 (2020), 1902714.
[22] T.R. Cook, D.K. Dogutan, S.Y. Reece, Y. Surendranath, T.S. Teets, D.G. Nocera, Solar energy supply and storage for the legacy and nonlegacy worlds, Chem. Rev. 110 (2010) 6474–6502.
[23] C.M.A. Parlett, K. Wilson, A.F. Lee, Hierarchical porous materials: catalytic applications, Chem. Soc. Rev. 42 (2013) 3876–3893.
[24] L. Yang, H. Ren, Q. Liang, K.N. Dinh, R. Dangol, Q. Yan, Ultrathin amorphous nickel doped cobalt phosphates with highly ordered mesoporous structures as efficient electrocatalyst for oxygen evolution reaction, Small 16 (2020), 1906766.
[25] J. Zhang, T. Wang, P. Liu, Z. Liao, S. Liu, X. Zhuang, M. Chen, E. Zschech, X. Feng, Efficient hydrogen production on MoNi4 electrocatalysts with fast water dissociation kinetics, Nat. Commun. 8 (2017) 15437.
[26] S. Anantharaj, S. Noda, M. Driess, P.W. Menezes, The pitfalls of using potentiodynamic polarization curves for tafel analysis in electrocatalytic water splitting, ACS Energy Lett. 6 (2021) 1607–1611.
[27] J.G. Chen, C.W. Jones, S. Linic, V.R. Stamenkovic, Best practices in pursuit of topics in heterogeneous electrocatalysis, ACS Catal. 7 (2017) 6392–6393.
[28] C. Wei, R.R. Rao, J. Peng, B. Huang, I.E.L. Stephens, M. Risch, Z.J. Xu, Y. Shao-Horn, Recommended practices and benchmark activity for hydrogen and oxygen electrocatalysis in water splitting and fuel cells, Adv. Mater. 31 (2019), 1806296.
[29] S. Anantharaj, S.R. Ede, K. Karthick, S. Sam Sankar, K. Sangeetha, P.E. Karthik, S. Kundu, Precision and correctness in the evaluation of electrocatalytic water splitting: revisiting activity parameters with a critical assessment, Energy Environ. Sci. 11 (2018) 744–771.
[30] M. Görlin, P. Chernev, J. Ferreira de Araújo, T. Reier, S. Dresp, B. Paul, R. Krähnert, H. Dau, P. Strasser, Oxygen evolution reaction dynamics, faradaic charge efficiency, and the active metal redox states of ni–fe oxide water splitting electrocatalysts, J. Am. Chem. Soc. 138 (2016) 5603–5614.
[31] Y. Leng, G. Chen, A.J. Mendoza, T.B. Tighe, M.A. Hickner, C.-Y. Wang, Solid-state water electrolysis with an alkaline membrane, J. Am. Chem. Soc. 134 (2012) 9054–9057.
[32] J. Xiao, A.M. Oliveira, L. Wang, Y. Zhao, T. Wang, J. Wang, B.P. Setzler, Y. Yan, Water-fed hydroxide exchange membrane electrolyzer enabled by a fluoride-incorporated nickel–iron oxyhydroxide oxygen evolution electrode, ACS Catal. 11 (2021) 264–270.
[33] Q. Wang, H. Zhao, F. Li, W. She, X. Wang, L. Xu, H. Jiao, Mo-doped Ni2P hollow nanostructures: highly efficient and durable bifunctional electrocatalysts for alkaline water splitting, J. Mater. Chem. A 7 (2019) 7636–7643.
[34] T. Wang, Z. Jiang, K.H. Chu, D. Wu, B. Wang, H. Sun, H.Y. Yip, T. An, H. Zhao, P. K. Wong, X-shaped α-FeOOH with enhanced charge separation for visible-light-driven photocatalytic overall water splitting, ChemSusChem 11 (2018) 1365–1373.
[35] H. Li, X. Wang, Z. Zhao, Z. Tian, D. Zhang, Y. Wu, Ni2P nanoflake array/three dimensional graphene architecture as integrated free-standing anode for boosting the sodiation capability and stability, ChemElectroChem 6 (2019) 404–412.
[36] B. Seo, D.S. Baek, Y.J. Sa, S.H. Joo, Shape effects of nickel phosphide nanocrystals on hydrogen evolution reaction, CrystEngComm 18 (2016) 6083–6089.
[37] F. Yu, H. Zhou, Y. Huang, J. Sun, F. Qin, J. Bao, W.A. Goddard, S. Chen, Z. Ren, High-performance bifunctional porous non-noble metal phosphide catalyst for overall water splitting, Nat. Commun. 9 (2018) 2551.
[38] B. You, N. Jiang, M. Sheng, M.W. Bhushan, Y. Sun, Hierarchically porous urchin-like Ni2P superstructures supported on nickel foam as efficient bifunctional electrocatalysts for overall water splitting, ACS Catal. 6 (2016) 714–721.
[39] Z. Hu, Z. Shen, J.C. Yu, Covalent fixation of surface oxygen atoms on hematite photoanode for enhanced water oxidation, Chem. Mater. 28 (2016) 564–572.
[40] S. Klaus, Y. Cai, M.W. Louie, L. Trotochaud, A.T. Bell, Effects of Fe electrolyte impurities on Ni(OH)2/NiOOH structure and oxygen evolution activity, J. Phys. Chem. 119 (2015) 7243–7254.
[41] M.W. Louie, A.T. Bell, An investigation of thin-film Ni–Fe oxide catalysts for the electrochemical evolution of oxygen, J. Am. Chem. Soc. 135 (2013) 12329–12337.
[42] Y. Li, C. Zhao, Iron-doped nickel phosphate as synergistic electrocatalyst for water oxidation, Chem. Mater. 28 (2016) 5659–5666.
[43] D. Friebel, M.W. Louie, M. Bajdich, K.E. Sanwald, Y. Cai, A.M. Wise, M.-J. Cheng, D. Sokaras, T.-C. Weng, R. Alonso-Mori, R.C. Davis, J.R. Bargar, J.K. Nørskov, A. Nilsson, A.T. Bell, Identification of highly active Fe sites in (Ni,Fe)OOH for electrocatalytic water splitting, J. Am. Chem. Soc. 137 (2015) 1305–1313.
[44] C. Wei, Z.J. Xu, The comprehensive understanding of as an evaluation parameter for electrochemical water splitting, small, Methods 2 (2018), 1800168.
[45] M.B. Stevens, L.J. Enman, A.S. Batchellor, M.R. Cosby, A.E. Vise, C.D.M. Trang, S. W. Boettcher, Measurement techniques for the study of thin film heterogeneous water oxidation electrocatalysts, Chem. Mater. 29 (2017) 120–140.
[46] H. Xiao, H. Shin, W.A. Goddard, Synergy between Fe and Ni in the optimal performance of (Ni,Fe)OOH catalysts for the oxygen evolution reaction, Proc. Natl. Acad. Sci. U.S.A. 115 (2018) 5872.
[47] X. Zhao, B. Pattengale, D. Fan, Z. Zou, Y. Zhao, J. Du, J. Huang, C. Xu, Mixed-node metal–organic frameworks as efficient electrocatalysts for oxygen evolution reaction, ACS Energy Lett. 3 (2018) 2520–2526.
[48] A. Dutta, S. Mutyala, A.K. Samantara, S. Bera, B.K. Jena, N. Pradhan, Synergistic effect of inactive iron oxide core on active nickel phosphide shell for significant enhancement in oxygen evolution reaction activity, ACS Energy Lett. 3 (2018) 141–148.
[49] C.C.L. McCrory, S. Jung, J.C. Peters, T.F. Jaramillo, Benchmarking heterogeneous electrocatalysts for the oxygen evolution reaction, J. Am. Chem. Soc. 135 (2013) 16977–16987.
[50] A. Dutta, N. Pradhan, Developments of metal phosphides as efficient OER precatalysts, J. Phys. Chem. 8 (2017) 144–152.
[51] J. Chang, Y. Xiao, M. Xiao, J. Ge, C. Liu, W. Xing, Surface oxidized cobalt-phosphide nanorods as an advanced oxygen evolution catalyst in alkaline solution, ACS Catal. 5 (2015) 6874–6878.
[52] Z. Weng, W. Liu, L.-C. Yin, R. Fang, M. Li, E.I. Altman, Q. Fan, F. Li, H.-M. Cheng, H. Wang, Metal/oxide interface nanostructures generated by surface segregation for electrocatalysis, Nano Lett. 15 (2015) 7704–7710.
[53] L.-A. Stern, L. Feng, F. Song, X. Hu, Ni2P as a Janus catalyst for water splitting: the oxygen evolution activity of Ni2P nanoparticles, Energy Environ. Sci. 8 (2015) 2347–2351.
[54] J. Xu, J.P.S. Sousa, N.E. Mordvinova, J.D. Costa, D.Y. Petrovykh, K. Kovnir, O. I. Lebedev, Y.V. Kolen'ko, Al-induced in situ formation of highly active nanostructured water-oxidation electrocatalyst based on Ni-phosphide, ACS Catal. 8 (2018) 2595–2600.
[55] B. Song, K. Li, Y. Yin, T. Wu, L. Dang, M. Cabán-Acevedo, J. Han, T. Gao, X. Wang, Z. Zhang, J.R. Schmidt, P. Xu, S. Jin, Tuning mixed nickel iron phosphosulfide nanosheet electrocatalysts for enhanced hydrogen and oxygen evolution, ACS Catal. 7 (2017) 8549–8557.
[56] W. Chen, Y. Liu, Y. Li, J. Sun, Y. Qiu, C. Liu, G. Zhou, Y. Cui, In situ electrochemically derived nanoporous oxides from transition metal dichalcogenides for active oxygen evolution catalysts, Nano Lett. 16 (2016) 7588–7596.
[57] W. Chen, H. Wang, Y. Li, Y. Liu, J. Sun, S. Lee, J.-S. Lee, Y. Cui, In situ electrochemical oxidation tuning of transition metal disulfides to oxides for enhanced water oxidation, ACS Cent. Sci. 1 (2015) 244–251.
[58] B.R. Wygant, K. Kawashima, C.B. Mullins, Catalyst or precatalyst? the effect of oxidation on transition metal carbide, pnictide, and chalcogenide oxygen evolution catalysts, ACS Energy Lett. 3 (2018) 2956–2966.
[59] D.E. Hall, Alkaline water electrolysis anode materials, J. Electrochem. Soc. 132 (1985) 41C.
[60] R.D.L. Smith, M.S. Prévot, R.D. Fagan, Z. Zhang, P.A. Sedach, M.K.J. Siu, S. Trudel, C.P. Berlinguette, Photochemical route for accessing amorphous metal oxide materials for water oxidation catalysis, Science 340 (2013) 60.